Chinese Journal of Aeronautics, (2014),27(6): 1401–1412

Chinese Society of Aeronautics and Astronautics
& Beihang University

Chinese Journal of Aeronautics

cja@buaa.edu.cn
www.sciencedirect.com

Analytic estimation and numerical modeling of actively cooled thermal protection systems with nickel alloys

Wang Xinzhi [a], He Yurong [a,*], Zheng Yan [a], Ma Junjun [b], H. Inaki Schlaberg [c]

[a] *School of Energy Science and Engineering, Harbin Institute of Technology, Harbin 15000, China*
[b] *Shanxi Blower (Group) Company Limited, Xi'an 710082, China*
[c] *School of Control and Computer Engineering, North China Electric Power University, Beijing 102206, China*

Received 19 December 2013; revised 15 February 2014; accepted 15 April 2014
Available online 18 October 2014

KEYWORDS

Active cooling;
Electric analogy method;
Nickel alloys;
Thermal barrier coatings;
Thermal protection systems

Abstract Actively cooled thermal protection system has great influence on the engine of a hypersonic vehicle, and it is significant to obtain the thermal and stress distribution in the system. So an analytic estimation and numerical modeling are performed in this paper to investigate the behavior of an actively cooled thermal protection system. The analytic estimation is based on the electric analogy method and finite element analysis (FEA) is applied to the numerical simulation. Temperature and stress distributions are obtained for the actively cooled channel walls with three kinds of nickel alloys with or with no thermal barrier coating (TBC). The temperature of the channel wall with coating has no obvious difference from the one with no coating, but the stress with coating on the channel wall is much smaller than that with no coating. Inconel X-750 has the best characteristics among the three Ni-based materials due to its higher thermal conductivity, lower elasticity module and greater allowable stress. Analytic estimation and numerical modeling results are compared with each other and a reasonable agreement is obtained.

1. Introduction

The high specific impulse enabled by air-breathing engines is a key factor in the technology for the continued development of advanced high-Mach-number aerospace flight systems. The aerothermodynamic characteristics of scramjet engines have been extensively researched, and their potential was successfully demonstrated. However, for parts of the hypersonic vehicle design, there is an urgent need for strong, lightweight, high-temperature and oxidation-resistant structures.[1–3] The combustor must endure extremely demanding

* Corresponding author. Tel.: +86 451 86413233.
E-mail addresses: wangxz@hit.edu.cn (X. Wang), rong@hit.edu.cn (Y. He).

Peer review under responsibility of Editorial Committee of CJA.

Production and hosting by Elsevier

http://dx.doi.org/10.1016/j.cja.2014.10.006

high-temperatures (near 1000 °C) and oxidation conditions when operating at Mach 7 cruise conditions.[4–6] An actively cooled thermal protection system is a good choice to solve this problem. When the active cooling fuel flows across the panels of a combustor wall, the temperature of the engine reduces while the temperature of the fuel rises, which will improve the operating condition of the hypersonic vehicle. Continuously repeated channels of these panel-fuel-panel sandwiches allow internal fluid transport and enable simultaneous active cooling.[7–10] Due to nickel-based superalloys' high resistance to damage and the availability of relatively low-cost manufacturing approaches, they are widely used in high-temperature aerospace applications.[11–17]

Duplication of the hypersonic flight environment requires extreme temperatures and pressures coupled with complex physical interactions. So the testing and evaluation of hypersonic systems presents a unique set of challenges. Rakow and Waas[18,19] introduced and validated a novel experimental technique and load frame, which provides a significant improvement in the simultaneous preservation of thermal and mechanical boundary conditions during thermomechanical structural testing, and used it to evaluate sandwich panels with metal foam cores which are applied as actively cooled thermal protection systems in hypersonic vehicles. Langener et al.[20] used a supersonic hot-gas-flow test facility to investigate the application of transpiration cooling to ceramic matrix composite materials for scramjets. Song et al.[21] performed a transpiration cooling experiment using an optical heating method that provides a heat flux as high as 234 W/cm^2 on the surface of a specimen for a scramjet engine. Qin et al.[22–24] established a testing system and conducted an experimental study on the operating characteristics and performance of the re-cooling cycle of a hydrocarbon fueled scramjet engine with different flow, heat transfer and cracking conditions. Kumar et al.[25] investigated the thermal profile of a sandwich-type metallic thermal protection system filled with insulation over a period of 1000 s of experiments.

Ground-test facilities are limited in their ability to duplicate all salient parameters simultaneously. Datasets from flight experimentation are also limited due to airspace range requirements for long-distance flight corridors.[26] Computational techniques are a growing supplement to experiment; however, analytical models and computational techniques are extremely time-consuming, falling short of adequate fidelity, and requiring data to anchor and validate them.

Lu et al.[7] used numerical simulations to get the thermal characteristics of all-metallic sandwich structures with two-dimensional prismatic and truss cores. Vermaak et al.[27–30] developed a new processing method to study the high-temperature performance of actively cooled vapor phase strengthened nickel-based thermostructural panels and established a computational technique to determine shakedown limits for actively cooled structures that withstand extreme thermomechanical loads. Valdevit et al.[31–33] developed a material selection methodology for actively cooled rectangular panels. The procedure incorporates an analytical model for temperature and stress distributions subject to thermomechanical loads representative of hypersonic flight conditions. Pizzarelli et al.[34,35] analyzed the effect of wall heat conduction on the coolant flow by means of coupled computations between a validated Reynolds-averaged Navier–Stokes equations solver for the coolant flow field and a Fourier's equation solver for the thermal conduction in the solid material. Kontinos[36] coupled a thermal analysis method with application to metallic thermal protection panels. Bao et al.[37,38] proposed a 1D cooling channel model using unsteady partial differential equations (PDEs) and taking into account the strong dependencies of hydrocarbon fuel properties on temperature and pressure.

The literature review performed by the present authors did not yield a definite model that can properly considers the coolant flow and thermomechanical loads for actively cooled thermal protection systems with nickel alloys. As a result, the objective of this study is to establish an analytic estimation model to investigate actively cooled structures that withstand extreme thermomechanical loads. Actively cooled systems with three kinds of nickel alloys with and with no thermal barrier coating (TBC) are investigated with this model and temperature and stress distributions are obtained.

2. Model

2.1. Physical model

A typical hypersonic vehicle is shown in Fig. 1, in which we can see that the combustion chamber is surrounded by sandwich panels. The detailed structures of the sandwich panels are shown in Fig. 2. The actively cooled panels suffer extremely high thermal loads from the combustion chamber.

2.2. Thermal analysis

Four assumptions are used in this work to investigate the temperature distribution of the active cooling system, which are shown as follows:

(1) The top face of the panel is exposed to hot gases at a uniform adiabatic wall temperature T_{aw} and constant convective heat transfer coefficient h_G.
(2) The bottom face and the sides are thermally insulated. All heat from the top face is carried away by the cooling fluid.
(3) The heat conduction along the length of the panel in both the channel structure and the coolant is ignored.
(4) The coolant temperature is uniform at each cross section, increasing with distance Z along the panel length from an initial value T_{f0} at the channel inlet to its maximum T_{fmax} at the outlet.

We select one panel unit as the analysis unit since the actively cooled panel structure is repeated periodically. The thermal resistance network is shown in Fig. 3, where

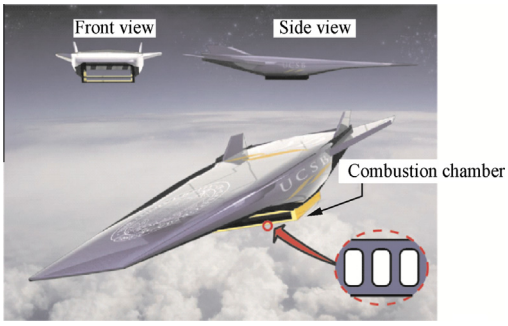

Fig. 1 A typical hypersonic vehicle photo.[32]

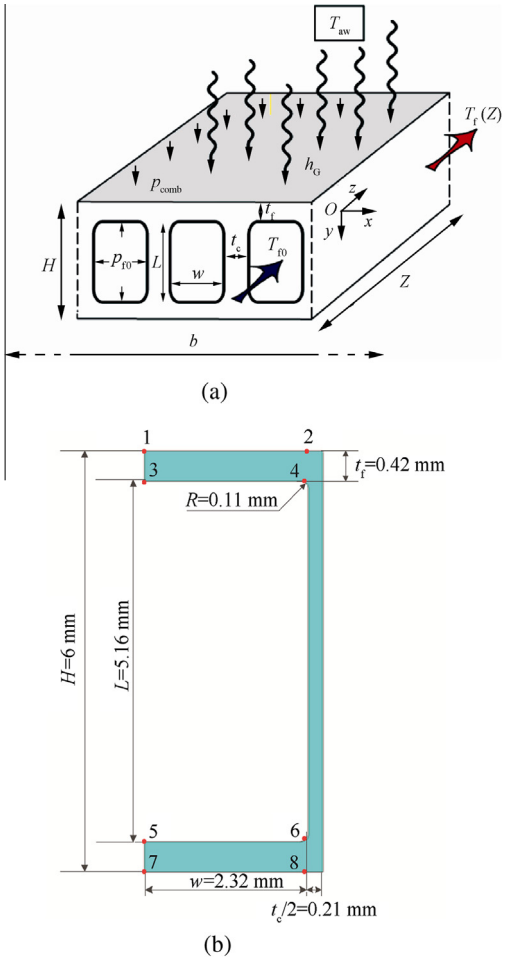

Fig. 2 Structures of the actively cooled system. (a) Schematic of thermo-structural loads, variable definitions and coordinate system.[32] (b) Detailed structure of the outlet cross section.

top face/hot gas boundary: $R_G = 1/h_G$
across the TBC (when present): $R_{TBC} = t_{TBC}/k_{TBC}$
across the hot face (y-direction): $R_{face} = t_f/k_s$
along the hot face (x-direction): $R_h = (w + t_c/2)/(4k_s)$
top face/coolant boundary: $R_{cool} = 1/h_c$
core web (modeled as a 1D thermal fin)[31,36]: $R_{fin} = \left(\sqrt{\frac{2h_c}{k_s t_c}}k_s\right)^{-1} \operatorname{artanh}\sqrt{\frac{2h_c}{k_s t_c}L^2}$

where R is the thermal resistance, k_s is the thermal conductivity of the panel material, k_{TBC} is the thermal conductivity of the TBC, h_c is heat transfer coefficient on the coolant side, t is the thickness of the wall; subscript c means core web, subscript f means face sheet; w is the width of cooling channel, and L is height of cooling channel.

The model can be simplified into the effective network of Fig. 3, where T means the temperature, subscript tfc means the location on the top side of the top face away from a core web, subscript tfw means the location on the top side of the top face over a core web, T_f means the average temperature of the fuel at the cross section of the channel; q_w means the heat flux into the web, q_c means the heat flux convected from the top face into the coolant and q_h horizontal heat flux in the top face. This model characterized by four resistances, R_1, R_{2w}, R_{2c}, R_h, where $R_1 = R_G + R_{face}/2$, $R_{2w} = R_{cool} + R_{face}/2$, $R_{2c} = R_{fin} + R_{face}/2$. Further simplifying, we can get the effective network as shown in Fig. 4.

Based on the analogy of circuit analysis, five equations are obtained for each circuit.

$$\begin{cases} T_{aw} - T_f = q_w R_1 + (q_w + 2q_h t_f/w)R_{2w} \\ T_{aw} - T_f = q_c R_1 + (q_c - 2q_h t_f/t_c)R_{2c} \\ T_{aw} - T_{tfw} = q_w R_1 \\ T_{aw} - T_{tfc} = q_c R_1 \\ T_{tfc} - T_{tfw} = q_h R_h \end{cases} \tag{1}$$

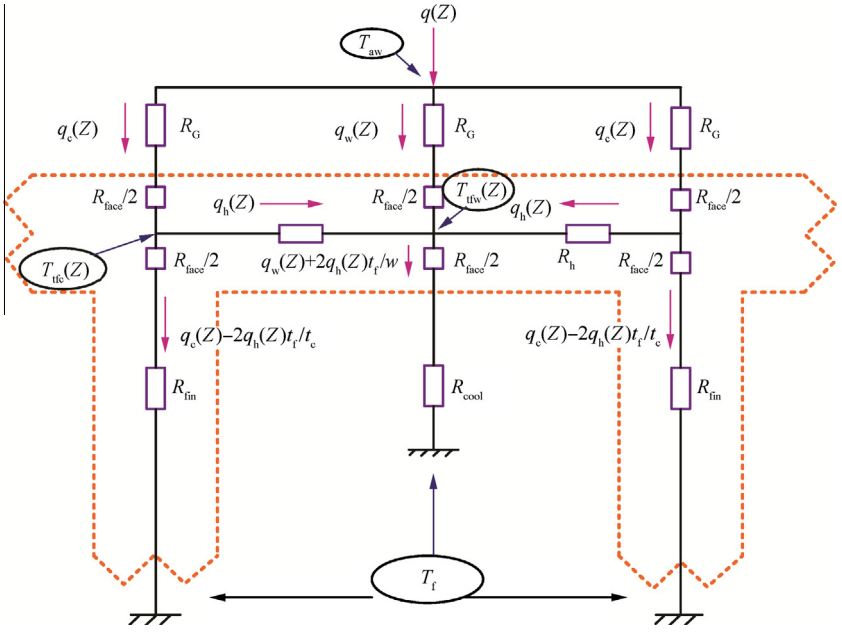

Fig. 3 Schematic of thermal resistance network.

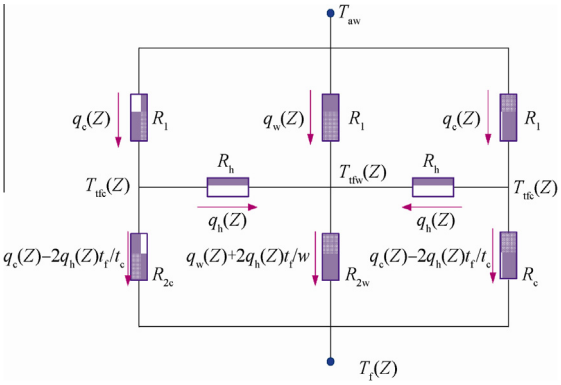

Fig. 4 Schematic of effective network.

Then the heat fluxes can be obtained as

$$\begin{cases} q_c = \dfrac{T_{aw} - T_f}{R_1} R_{c^*} \\ q_w = \dfrac{T_{aw} - T_f}{R_1} R_{w^*} \\ q_h = \dfrac{T_{aw} - T_f}{R_1} R_{h^*} \end{cases} \tag{2}$$

where

$$\begin{cases} R_{w^*} = \dfrac{R_1[R_{2c}R_h + R_1(R_h + 2R_{2c}t_f/t_c + 2R_{2w}t_f/w)]}{a} \\ R_{c^*} = \dfrac{R_1[R_{2w}R_h + R_1(R_h + 2R_{2c}t_f/t_c + 2R_{2w}t_f/w)]}{a} \\ R_{h^*} = \dfrac{R_1^2(R_{2c} - R_{2w})}{a} \\ a = R_{2c}R_{2w}R_h + R_1^2(R_h + 2R_{2c}t_f/t_c + 2R_{2w}t_f/w) \\ \quad + R_1\{R_{2w}R_h + R_{2c}[R_h + 2R_{2w}(t_f/t_c + t_f/w)]\} \end{cases} \tag{3}$$

The temperature of the coolant can be obtained by energy balance equation

$$\rho_f c_{p,f} V^{eff} \frac{dT}{dz} = \frac{w q_w(Z) + t_c q_c(Z)}{w + t_c} \tag{4}$$

where $\rho_f c_{p,f}$ is the volumetric specific heat, V^{eff} is the volumetric fuel flow rate per unit width of the panel, z means the coordinate and Z means the length along the z. The left side of Eq. (4) calculates the heat absorption of the coolant and the right side of Eq. (4) presents the heat transfer to the coolant.

Combining Eq. (4) with Eq. (2) we can get

$$\frac{d(T_{aw} - T_f)}{dz} + \frac{1}{R_1 \rho_f c_{p,f} V^{eff}} \left(\frac{w}{w + t_c} R_{w^*} + \frac{t_c}{w + t_c} R_{c^*} \right) (T_{aw} - T_f) = 0 \tag{5}$$

Then we can obtain

$$\frac{T_{aw} - T_f}{T_{aw} - T_{f0}} = \exp(-\beta z) \tag{6}$$

where

$$\beta = \frac{1}{R_1 \rho_f c_{p,f} V^{eff}} \left(\frac{w}{w + t_c} R_{w^*} + \frac{t_c}{w + t_c} R_{c^*} \right) \tag{7}$$

and T_f is the average temperature of the coolant at the cross section of the channel.

Based on the relationship between the temperature difference, heat flux and thermal resistance, the temperatures at points 1–8 in Fig. 2 are as follows:

$$\begin{cases} T_1 = T_{aw} - (T_{aw} - T_{tfw})\left(1 - \dfrac{1}{2} \cdot \dfrac{R_{face}}{R_1}\right) \\ T_2 = T_{aw} - (T_{aw} - T_{tfc})\left(1 - \dfrac{1}{2} \cdot \dfrac{R_{face}}{R_1}\right) \\ T_3 = T_{aw} - \left[(T_{aw} - T_{tfw}) + \dfrac{1}{2} R_{face}\left(q_w + 2q_h \dfrac{t_f}{w}\right)\right] \\ T_4 = T_{aw} - \left[(T_{aw} - T_{tfc}) + \dfrac{1}{2} R_{face}\left(q_c - 2q_h \dfrac{t_f}{t_c}\right)\right] \\ T_{5-8} = T_{aw} - \left[T_{aw} - T_f - \dfrac{\theta(L)}{\theta_0} R_{fin} q_c - 2q_h \dfrac{t_f}{t_c}\right] \\ T_{fin} = T_{aw} - \left[T_{aw} - T_f - \dfrac{\theta(y)}{\theta_0} R_{fin}\left(q_c - 2q_h \dfrac{t_f}{t_c}\right)\right] \end{cases} \tag{8}$$

Combined with the above analysis, the temperatures at points 1–8 can be expressed as

$$\begin{cases} T_1 = T_{aw} - (T_{aw} - T_{f0})\left(1 - \dfrac{1}{2} \cdot \dfrac{R_{face}}{R_1}\right) R_{w^*} \exp(-\beta z) \\ T_2 = T_{aw} - (T_{aw} - T_{f0})\left(1 - \dfrac{1}{2} \cdot \dfrac{R_{face}}{R_1}\right) R_{c^*} \exp(-\beta z) \\ T_3 = T_{aw} - (T_{aw} - T_{f0})\left[R_{w^*} + \left(\dfrac{1}{2} R_{w^*} + R_{h^*} \dfrac{t_f}{w}\right) \dfrac{R_{face}}{R_1}\right] \exp(-\beta z) \\ T_4 = T_{aw} - (T_{aw} - T_{f0})\left[R_{c^*} + \left(\dfrac{1}{2} R_{c^*} - R_{h^*} \dfrac{t_f}{t_c}\right) \dfrac{R_{face}}{R_1}\right] \exp(-\beta z) \\ T_{5-8} = T_{aw} - (T_{aw} - T_{f0})\left[1 - \dfrac{\theta(L)}{\theta_0} \cdot \dfrac{R_{fin}}{R_1}\left(R_{c^*} - 2R_{h^*} \dfrac{t_f}{t_c}\right)\right] \exp(-\beta z) \\ T_{fin} = T_{aw} - (T_{aw} - T_{f0})\left[1 - \dfrac{\theta(y)}{\theta_0} \cdot \dfrac{R_{fin}}{R_1}\left(R_{c^*} - 2R_{h^*} \dfrac{t_f}{t_c}\right)\right] \exp(-\beta z) \end{cases} \tag{9}$$

where

$$\frac{\theta(y)}{\theta_0} = \frac{T(y) - T_f}{T(0) - T_f} = \frac{\cosh \sqrt{\dfrac{2h_c}{k_s t_c}}(L - y)}{\cosh \sqrt{\dfrac{2h_c}{k_s t_c}} L} \tag{10}$$

where $\theta(y)/\theta_0$ is the nondimensional fin temperature, and $T(y)$ the temperature at the fin along the y coordinate, $T(0)$ is the temperature at the bottom point in the fin.

2.3. Stress analysis

Plate bending and stretching theory is used in this work to estimate the stress assuming the materials to be of linear elasticity. The total stress consists of thermal and mechanical stresses.

Temperature difference induces the thermal stress in the panel. The main temperature differences are

$$\frac{\Delta T_{tfc}}{T_{aw} - T_{f0}} = \frac{T_2 - T_4}{T_{aw} - T_{f0}} = \left(R_{c^*} - R_{h^*} \frac{t_f}{t_c}\right) \frac{R_{face}}{R_1} \exp(-\beta z) \tag{11}$$

$$\frac{\Delta T_{tfw}}{T_{aw} - T_{f0}} = \frac{T_1 - T_3}{T_{aw} - T_{f0}} = \left(R_{w^*} + R_{h^*} \frac{t_f}{w}\right) \frac{R_{face}}{R_1} \exp(-\beta z) \tag{12}$$

$$\frac{\Delta T_{pc}}{T_{aw} - T_{f0}} = \frac{T_4 - T_5}{T_{aw} - T_{f0}} = \left[\frac{R_{2c}}{R_1} - \frac{R_{fin}}{R_1} \cdot \frac{\theta(L)}{\theta_0}\right] \left(R_{c^*} - 2R_{h^*} \frac{t_f}{t_c}\right) \exp(-\beta z) \tag{13}$$

$$\frac{\Delta T_{\mathrm{pw}}}{T_{\mathrm{aw}}-T_{\mathrm{f0}}}=\frac{T_3-T_5}{T_{\mathrm{aw}}-T_{\mathrm{f0}}}=\left[\left(R_{\mathrm{w}^*}+2R_{\mathrm{h}^*}\frac{t_{\mathrm{f}}}{w}\right)\frac{R_{2\mathrm{w}}}{R_1}-\left(R_{\mathrm{c}^*}-2R_{\mathrm{h}^*}\frac{t_{\mathrm{f}}}{t_{\mathrm{c}}}\right)\frac{R_{\mathrm{fin}}}{R_1}\cdot\frac{\theta(L)}{\theta_0}\right]\exp(-\beta z) \tag{14}$$

where ΔT_{tfc}, ΔT_{tfw}, ΔT_{pc} and ΔT_{pw} mean the temperature difference across the top face away from the core web, across the top face above a core web, the panel away from the core web, and across the panel above a core web respectively.

According to the Ref. [39], thermal stress has a relationship with temperature difference and the properties of materials. The temperature difference across the top face causes compression along its top surface and tension along its bottom surface. These stresses are

$$\sigma_x^{\Delta T_{\mathrm{tf}}}=\sigma_y^{\Delta T_{\mathrm{tf}}}=\begin{cases}-\dfrac{E\alpha\Delta T_{\mathrm{tf}}}{2(1-\nu)} & \text{points } 1,2\\ \dfrac{E\alpha\Delta T_{\mathrm{tf}}}{2(1-\nu)} & \text{points } 3,4\end{cases} \tag{15}$$

where $\Delta T_{\mathrm{tf}}=\Delta T_{\mathrm{tfc}}$, σ is the stress, x and y are coordinates, ν is the Poisson's ratio, E and α are the Young's modulus and the coefficient of thermal expansion of the material, respectively. The average temperature difference between the top and bottom faces is $\Delta T_{\mathrm{p}}=(\Delta T_{\mathrm{pw}}+\Delta T_{\mathrm{pc}})/2$, which causes the panel to deform uniformly in the x and y directions and thus generates the compression in the top face and tension in the bottom face. Considering the stretching stiffness of the core members along the y direction and assuming the temperatures of the core and the bottom face as the same in the steady state, the resulting additional stresses are

$$\sigma_x^{\Delta T_{\mathrm{p}}}=\begin{cases}-\dfrac{E\alpha\Delta T_{\mathrm{p}}}{2(1-\nu)} & \text{points } 1,2,3,4\\ \dfrac{E\alpha\Delta T_{\mathrm{p}}}{2(1-\nu)} & \text{points } 5,6,7,8\end{cases} \tag{16}$$

$$\sigma_y^{\Delta T_{\mathrm{p}}}=\begin{cases}-\dfrac{E\alpha\Delta T_{\mathrm{p}}(A_{\mathrm{f}}+A_{\mathrm{c}})}{(1-\nu)(2A_{\mathrm{f}}+A_{\mathrm{c}})} & \text{points } 1,2,3,4\\ \dfrac{E\alpha\Delta T_{\mathrm{p}}A_{\mathrm{f}}}{(1-\nu)(2A_{\mathrm{f}}+A_{\mathrm{c}})} & \text{points } 5,6,7,8\end{cases} \tag{17}$$

where $A_{\mathrm{f}}=t_{\mathrm{f}}(w+t_{\mathrm{c}})$ and $A_{\mathrm{c}}=(H-2t_{\mathrm{f}})t_{\mathrm{c}}$.

The mechanical stress caused by the external pressure from the combustion gases p_{comb} is much less than the internal pressure from the coolant p_{f}, so the mechanical stress caused by the pressure on the top face can be ignored in this work. It is assumed that the bottom of the panel is fixed. In the x direction, the mechanical stresses $\sigma_x^{p_{\mathrm{f}}}$ caused by p_{f} can be divided by two parts at points 1–4. One part of the $\sigma_x^{p_{\mathrm{f}}}$ is caused by the pressure on the vertical side of the panel with a length of L, and the other part of the $\sigma_x^{p_{\mathrm{f}}}$ caused by the pressure on the horizontal side of the panel with a width of w, and the length of the cross section is $2t_{\mathrm{f}}$. Accord to Ref. [40], the first part of the $\sigma_x^{p_{\mathrm{f}}}$ can be calculated as

$$\frac{\sigma_x^{p_{\mathrm{f}}}}{p_{\mathrm{f}}}=L/(2t_{\mathrm{f}})\quad\text{points } 1,2,3,4 \tag{18}$$

The second part of the $\sigma_x^{p_{\mathrm{f}}}$ can be calculated as

$$\frac{\sigma_x^{p_{\mathrm{f}}}}{p_{\mathrm{f}}}=\begin{cases}(w/t_{\mathrm{f}})^2/4 & \text{point } 1\\ -(w/t_{\mathrm{f}})^2/2 & \text{point } 2\\ -(w/t_{\mathrm{f}})^2/4 & \text{point } 3\\ (w/t_{\mathrm{f}})^2/2 & \text{point } 4\end{cases} \tag{19}$$

So the mechanical stresses for these four points are as follows:

$$\frac{\sigma_x^{p_{\mathrm{f}}}}{p_{\mathrm{f}}}=\begin{cases}L/(2t_{\mathrm{f}})+(w/t_{\mathrm{f}})^2/4 & \text{point } 1\\ L/(2t_{\mathrm{f}})-(w/t_{\mathrm{f}})^2/2 & \text{point } 2\\ L/(2t_{\mathrm{f}})-(w/t_{\mathrm{f}})^2/4 & \text{point } 3\\ L/(2t_{\mathrm{f}})+(w/t_{\mathrm{f}})^2/2 & \text{point } 4\end{cases} \tag{20}$$

Then the mechanical stresses on the y direction can be calculated as

$$\frac{\sigma_y^{p_{\mathrm{f}}}}{p_{\mathrm{f}}}=\nu\frac{\sigma_x^{p_{\mathrm{f}}}}{p_{\mathrm{f}}}\quad\text{points } 1,2,3,4 \tag{21}$$

As the bottom face is displacement-limited, there pressure on the horizontal side does not affect the $\sigma_x^{p_f}$. So the mechanical stresses at bottom points are

$$\frac{\sigma_x^{p_{\mathrm{f}}}}{p_{\mathrm{f}}}=\frac{L}{2t_{\mathrm{f}}}\quad\text{points } 5,6,7,8 \tag{22}$$

$$\frac{\sigma_y^{p_{\mathrm{f}}}}{p_{\mathrm{f}}}=\nu\frac{\sigma_x^{p_{\mathrm{f}}}}{p_{\mathrm{f}}}\quad\text{points } 5,6,7,8 \tag{23}$$

2.4. Numerical method

A numerical simulation is also used to calculate the temperature and stress distribution in the actively cooled panel for comparison. The finite element analysis (FEA) method is applied to calculating the thermal/stress distributions.

2.4.1. Thermal model

The energy conservation equation is

$$\frac{\partial}{\partial x}\left(k\frac{\partial T}{\partial x}\right)+\frac{\partial}{\partial y}\left(k\frac{\partial T}{\partial y}\right)=0 \tag{24}$$

The third boundary condition applied in this model is expressed as

$$-k\left(\frac{\partial T}{\partial n}\right)_{\mathrm{w}}=h(T_{\mathrm{w}}-T_{\mathrm{l}}) \tag{25}$$

where k is the thermal conductivity, subscript w means wall and subscript l means liquid.

2.4.2. Stress model

The equation for the stress tensor is

$$\begin{cases}\dfrac{\partial\sigma_{xx}}{\partial x}+\dfrac{\partial\tau_{yx}}{\partial y}+X=0\\ \dfrac{\partial\tau_{xy}}{\partial x}+\dfrac{\partial\sigma_{yy}}{\partial y}+Y=0\end{cases} \tag{26}$$

$$\begin{bmatrix}\sigma_{xx}\\ \sigma_{yy}\\ \tau_{xy}\end{bmatrix}=\frac{E(1-\mu)}{(1+\mu)(1-2\mu)}\begin{bmatrix}1 & A_1 & 0\\ A_1 & 1 & 0\\ 0 & 0 & A_2\end{bmatrix}\begin{bmatrix}\varepsilon_{xx}-(1+\mu)\alpha\Delta T\\ \varepsilon_{yy}-(1+\mu)\alpha\Delta T\\ \gamma_{xy}\end{bmatrix} \tag{27}$$

where $\boldsymbol{\sigma}$ is the normal stress, $\boldsymbol{\tau}$ is the shear stress, $\boldsymbol{\varepsilon}$ is linear strain, $\boldsymbol{\gamma}$ is shear strain; $A_1=\mu/(1-\mu)$, $A_2=(1-2\mu)/[2(1-\mu)]$, μ is dynamic viscosity of the coolant.

2.4.3. Strength criterion

The Von Mises stress criterion is

$$\frac{1+\mu}{6E}\left[(\sigma_{xx}-\sigma_{yy})^2+\sigma_{yy}^2+\sigma_{xx}^2\right]\le\frac{1+\mu}{6E}\times 2\sigma_{\mathrm{s}}^2 \tag{28}$$

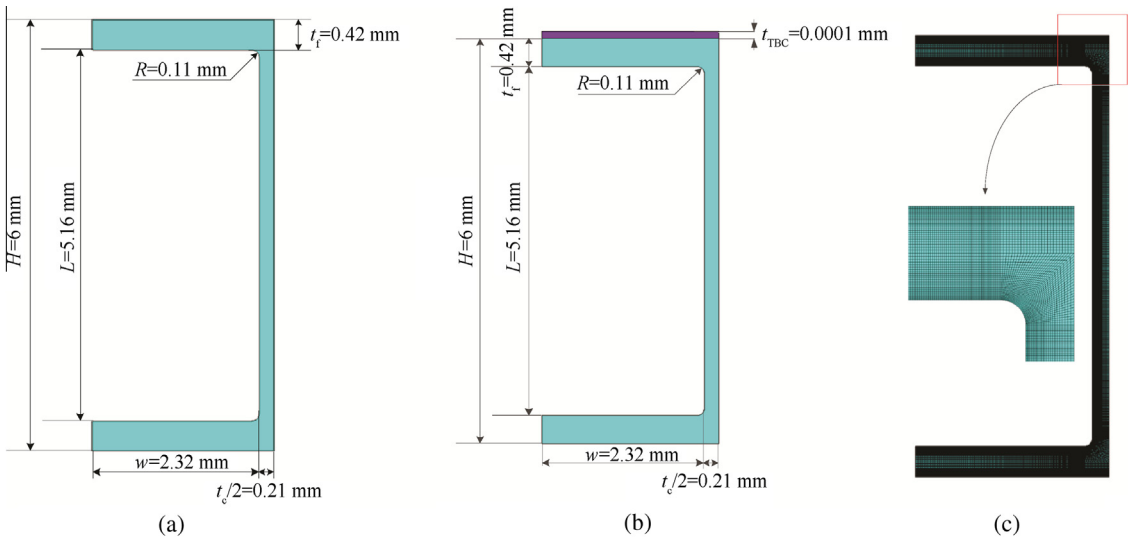

Fig. 5 Geometrical structure and the meshes for the cooling channel with and with no coating. (a) Cooling channel with no coating. (b) Cooling channel with coating. (c) FEM meshes.

$$\sigma = \sqrt{\sigma_{xx}^2 - \sigma_{xx}\sigma_{yy} + \sigma_{yy}^2} \le \sigma_s \tag{29}$$

where σ_s is the allowable stress.

2.4.4. Numerical object and meshes

After the previous analysis of the heat transfer of the whole combustion furnace in a 3D structure, a simplified 2D model is prepared in this part of the work. Here it is assumed that each cooling channel suffers the same load and that the temperature and stress reach their maximum values on the outer surface. Hence it is enough to analyze half of one cooling channel because of its symmetrical structure, as shown in Fig. 5(a) and (b) for the cases with no coating and with coating. Fig. 5(c) shows the meshes for the numerical simulation.

3. Initialization and boundary conditions

3.1. Materials

JP-7 is used as coolant in this work. It is made from petroleum fraction and is composed of hydrocarbons like alkane, cycloalkane and so on. It has been used as the main fuel for hypersonic vehicles. As it has a high endothermic capability, we use it as coolant for the active cooling system. As the hydrocarbons-fuel coolant flows through panels, the temperature of the solid decreases and the temperature of the coolant increases, and it is very helpful to the burning of the fuel. Its properties are shown in Table 1, where K_f, μ_f, c_p, ρ_f and T_{coke} mean the thermal conductivity, viscosity, specific heat capacity, density and coke temperature of the fuel, respectively; Pr_f is the Prandtl number of the fuel.

Nickel alloys are widely used in the aerospace field because of their high temperature resistance and high corrosion resistance. There are three types of nickel alloys that have been used as the solid material of the active cooling system. Their main physical properties are listed in Table 2, where T^*, σ_Y, $d\sigma/dT$, and ρ_s mean the maximum allowable temperature, yield strength, yield strength variation with temperature, and density of the solid materials, respectively.

ZrO_2 is an excellent refractory material. It is selected as the TBC to protect the actively cooled panels in this work. The main properties of ZrO_2 are listed in Table 3, where k_{TBC}, ρ_{TBC} are thermal conductivity, density of the ZrO_2.

3.2. Boundary conditions

As the engine of the hypersonic vehicle is complex, three assumptions are made in this work. Firstly, active cooling

Table 1 Properties of JP-7.

Fuel	K_f (W/(m·K))	μ_f (Pa·s)	c_p (J/(kg·K))	Pr_f	ρ_f (kg/m^3)	T_{coke} (K)
JP-7	0.11	1.984×10^{-4}	2575	4.64	800	975

Table 3 Properties of ZrO_2.

Material	k_{TBC} (W/(m·K))	ρ_{TBC} (kg/m^3)	E (GPa)	α (10^{-6}/K)	ν
ZrO_2	1.0	3000	190	10.3	0.36

Table 2 Properties of nickel alloy.

Material	T^* (K)	σ_Y (MPa)	$d\sigma/dT$ (MPa/K)	E (GPa)	α (10^{-6}/K)	k_s (W/(m·K))	ρ_s (kg/m^3)	c_p (J/(kg·K))
Inconel X-750	1100	795	−0.39	128	16.0	23.0	8276	430
Inconel 625	1100	427	−0.31	164	14.0	20.0	8440	430
Hastelloy X	1368	346	−0.1296	180	15.0	18.9	8220	461.95

Table 4 Analysis of temperature at main nodes of actively cooled panel with no TBC.

Material	Node temperature (K)							
	1	2	3	4	5	6	7	8
Inconel X-750	995.7	924.3	977.8	878.6	660.2	660.2	660.2	660.2
Inconel 625	1004.1	929.0	983.4	879.0	656.8	656.8	656.8	656.8
Hastelloy X	1007.5	931.0	985.6	879.2	655.6	655.6	655.6	655.6

has no effect on the combustion in the combustion chamber. The top face which attaches to the combustion chamber has constant adiabatic wall temperature T_{aw} and a constant convective heat transfer coefficient h_G. Secondly, no heat is conducted through the bottom face since it is at the side far of the combustion chamber.

As the actively cooled panels have a periodicity, only half a panel is selected for the analysis of thermal and stress distributions. In order to compare the theoretical and numerical results, the same thermal and mechanical boundary conditions are applied. These are as follows:

The top face: convection boundary condition. It is assumed that the combustion is in a stable state with an adiabatic temperature $T_{aw} = 3200$ K and a convective heat transfer coefficient $h_G = 500$ W/(m^2·K).

The inner face: convection boundary condition. The coolant takes the heat from the panel when it is flowing through the channel. Different mass flow rates result in different convective heat transfer coefficients of the inner face.

The bottom face: adiabatic boundary condition and no displacement limit in the y direction.

4. Results and discussion

4.1. Thermal analysis

The sizes of the actively cooled panel are chosen as $H = 0.006$ m, $L = 0.00516$ m, $b = 0.5$ m, $w = 0.00464$ m, $t_f = 0.00042$ m, $t_c = 0.00042$ m, equivalence ratio $\phi = 1.5$. For stoichiometric combustion the fuel flow rate (per unit width of combustor) is $V_{st} = 0.008$ m^2/s. Upon specifying dimensions, the effective flow rate per unit width of panel is $V_{st}^{eff} = V_{st}b/[2(b+H)] = 0.003$ m^2/s. Considering the equivalence ratio $\phi = 1.5$, the actual flow rate then becomes $V^{eff} = \phi \cdot V_{st}^{eff} = 0.0045$ m^2/s.

Three nickel-based alloys (Inconel X-750, Inconel 625, and Hastelloy X) are selected as the solid material choices for the panel. The temperatures at the key nodes of the actively cooled panel with Inconel X-750, Inconel 625, and Hastelloy X are listed in Table 4. From the table we can see that for all the three materials, the maximum temperature is at node 1 and the minimum temperature is at the bottom side of the panel.

By comparing the temperatures at node 1, node 2, node 3, and node 4, we find that the temperature decreases from the center of the panel towards the fin side in the part near the combustor. However, the temperature in this area is still very high, because a great amount of heat transfers from the combustion chamber to the coolant in this part. Moreover, the panel near the combustion chamber is exposed to the high temperature combustor, and therefore its temperature is higher than at the other side. In the part far from the combustor the temperature is very low. Due to reduced heat exchange in this part and the bottom face being thermally insulated, its temperature almost equals that of the coolant.

By comparing the temperatures at a same node with different materials we can see that the temperature in Inconel X-750 is lower than in Inconel 625 and Hastelloy X, and the temperature in Hastelloy X is the highest. The thermal conductivity has a great influence on the temperature distribution. As Inconel X-750 has the higher thermal conductivity and transfers heat to the coolant more easily, the temperature of Inconel X-750 is lower. The temperature differences are small.

The temperature at the key nodes with a TBC = 0.0001 m applied to the actively cooled panel, is shown in Table 5.

From Table 5 we can find that the temperatures of the actively cooled panel has a similar distribution, in which the highest temperature is at node 1 and the lowest temperature is at the bottom side of the panel. By comparing Tables 4 and 5, the temperature in the panel with TBC is lower than the temperature in the panel with no TBC at the same point. At the side near the combustion chamber the temperature with TBC is about 20 K lower than with no TBC. At the side far from the combustion chamber the temperature difference is about 10 K. This indicates that the TBC does provide some protection to the system.

A numerical method is used to simulate the temperature distribution in the actively cooled panels. The same materials and boundary conditions are considered in the simulation. In order to have a comparison, calculations for the panels with and with no TBC on the top face are performed.

The temperature distributions at the outlet cross section of the actively cooled panel with no TBC using different materials are shown in Fig. 6. Here we can see that the highest temperature is at the center of the top panel and decreases

Table 5 Analysis of temperature at main nodes of actively cooled panel with TBC.

Material	Node temperature (K)							
	1	2	3	4	5	6	7	8
Inconel X-750	972.7	903.9	955.5	860.0	649.9	649.9	649.9	649.9
Inconel 625	980.9	908.6	961.0	860.5	646.7	646.7	646.7	646.7
Hastelloy X	984.2	910.5	963.1	860.7	645.5	645.5	645.5	645.5

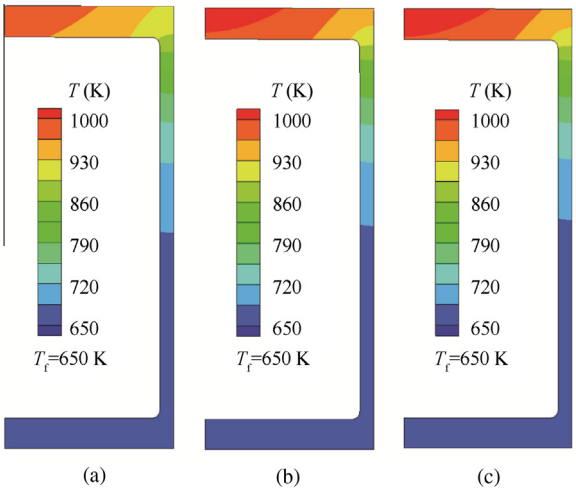

Fig. 6 Temperature distribution at the outlet cross section of actively cooled panel with no TBC. (a) Inconel X-750. (b) Inconel 625. (c) Hastelloy X.

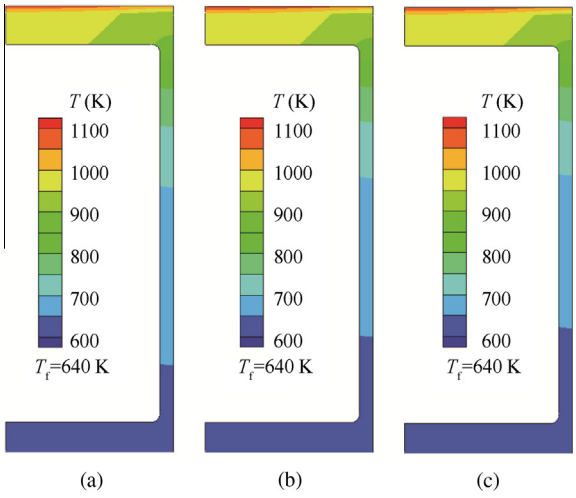

Fig. 7 Temperature distribution at the outlet cross section of actively cooled panel with TBC. (a) Inconel X-750. (b) Inconel 625. (c) Hastelloy X.

from the center towards the fin, and at the bottom side the panel temperature is almost equal to the fuel temperature.

The temperature distributions at the outlet cross section of the actively cooled panel with TBC and with different materials are shown in Fig. 7. A similar temperature distribution is found as in the panel with no TBC. But the temperature in Fig. 7 is lower than the temperature in Fig. 6 at the same point for the same material. It indicates that the TBC provides an effective protection for the actively cooled panel.

Since both the analytical and numerical methods can provide the temperature distribution for the panel of the cooling system and the analytical method saves around 80% of computing time, it is necessary to find out how well the results of these two methods agree with each other. Fig. 8 shows the comparison of the temperature distribution between the numerical and analytical results at the outlet cross section of the actively cooled panel with no and with TBC. The results show a reasonable agreement along the fin in y direction.

4.2. Stress analysis

The thermal stress and mechanical stress at the key nodes of the actively cooled panel without TBC using Inconel X-750, Inconel 625 and Hastelloy X are listed in Table 6. From the table we can see that the maximum thermal stress occurs at node 1 and the maximum mechanical stress happens at node 4 with all three materials.

Since the fuel pressure in the cooling channel stays constant, the mechanical stress at the various nodes is small and there is not a significant difference between the materials at the same nodes. However, the thermal stress for each node with the various materials is different because of the difference of thermal conductivity and elasticity module. Inconel X-750 has a relatively high thermal conductivity and a low elasticity module, so the Mises thermal stress is low at a same heat load.

As mentioned earlier, to protect the combustor, a TBC with a thickness of 0.1 mm is applied to the walls of the combustor. Table 7 shows the thermal stress and mechanical stress at the key nodes of the actively cooled panel with the TBC for Inconel X-750, Inconel 625 and Hastelloy X. We have already mentioned that with the application of the TBC, a temperature decrease of only 10–20 K is achieved, but the thermal stress for our three materials decreases both at the top and bottom walls. Hence, it indicates that the TBC can improve the thermal stress so as to protect the materials. Although the TBC improves the thermal stress distribution, it does little to improve the mechanical stress because it relies more on the pressure of the coolant.

A finite element method is also used to simulate the Mises stress for the cooling channel with no and with TBC. Fig. 9

Table 6 Analysis of stress at main nodes of actively cooled panel with no TBC.

Material		Node stress (MPa)							
		1	2	3	4	5	6	7	8
Inconel X-750	Thermal stress	578.0	578.0	548.9	548.9	563.4	563.4	563.4	563.4
	Mechanical stress	152.7	228.6	101.5	279.7	25.5	25.5	25.5	25.5
Inconel 625	Thermal stress	571.3	571.3	540.0	540.0	555.1	555.1	551.1	551.1
	Mechanical stress	153.5	229.8	102.0	281.3	25.7	25.7	25.7	25.7
Hastelloy X	Thermal stress	683.2	683.2	642.7	642.7	663.0	663.0	663.0	663.0
	Mechanical stress	154.0	230.5	102.4	282.1	25.8	25.8	25.8	25.8

Table 7 Analysis of stress at main nodes of actively cooled panel with TBC.

Material		Node stress (MPa)							
		1	2	3	4	5	6	7	8
Inconel X-750	Thermal stress	556.1	556.1	528.1	528.1	542.1	542.1	542.1	542.1
	Mechanical stress	152.7	228.6	101.5	279.7	25.6	25.6	25.6	25.6
Inconel 625	Thermal stress	549.7	549.7	518.6	518.6	534.2	534.2	534.2	534.2
	Mechanical stress	153.5	229.8	102.1	281.3	25.7	25.7	25.7	25.7
Hastelloy X	Thermal stress	657.5	657.5	618.5	618.5	637.9	637.9	637.9	637.9
	Mechanical stress	154.0	230.5	102.4	282.1	25.8	25.8	25.8	25.8

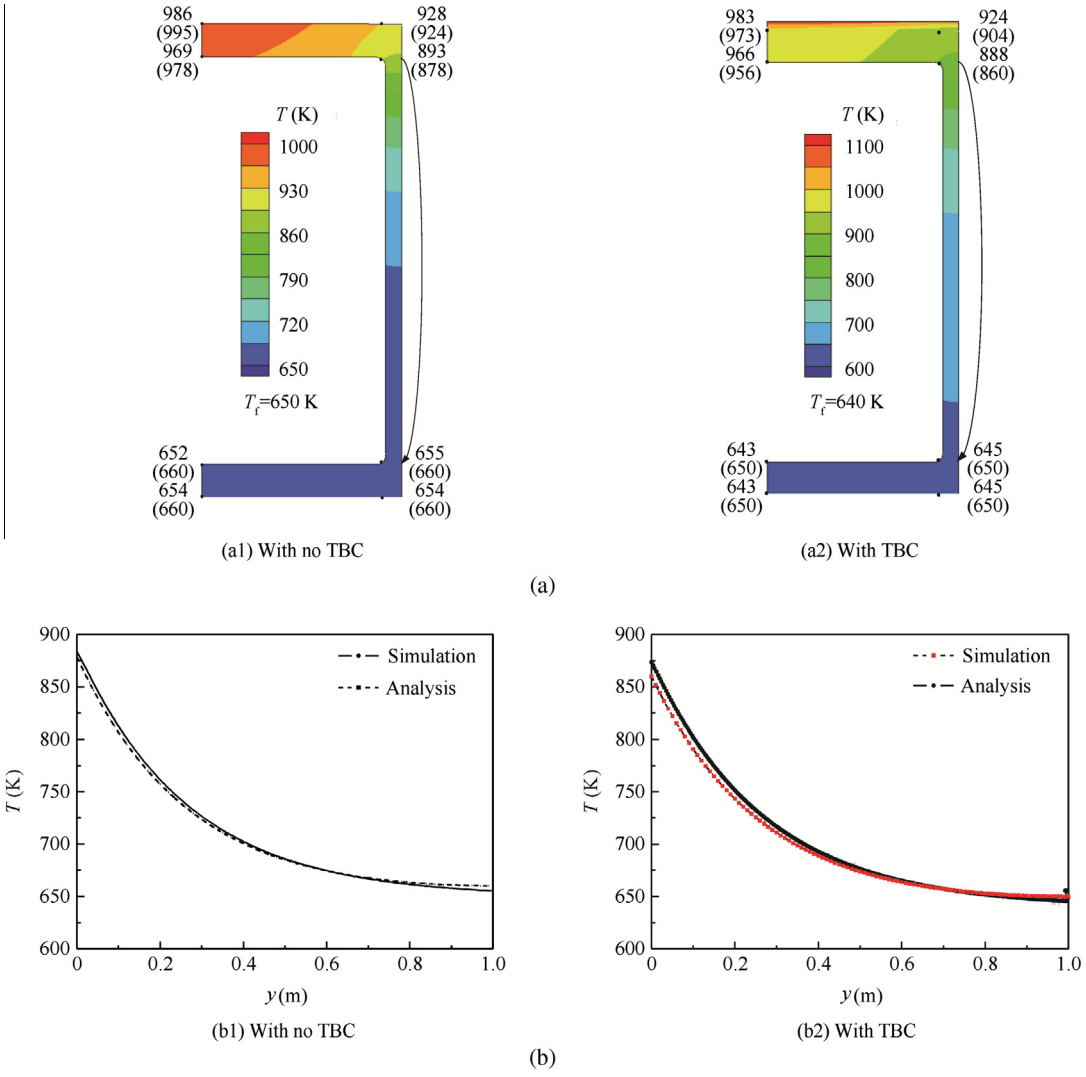

Fig. 8 Comparison of temperature distribution between numerical and analytical results at outlet cross section of actively cooled panel with no and with TBC. (a) Temperature distribution at the outlet cross section. (b) Temperature distribution along fin in y direction.

gives the numerical Mises stress distribution at the outlet cross section of the actively cooled panel with no TBC. It can be seen from the figure that the maximum Mises stress occurs at the top wall and the minimum value is in the upper middle part of the rib of the channel. From Table 2 we get that the allowable stress for the materials Inconel X-750, Inconel 625 and Hastelloy X are 795 MPa, 427 MPa and 346 MPa. In this case only the Mises stress of Inconel X-750 is lower than its

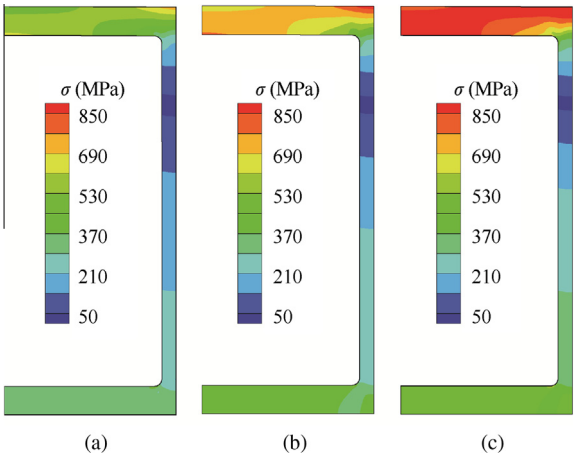

Fig. 9 Mises stress distribution at outlet cross of actively cooled panel with no TBC. (a) Inconel X-750. (b) Inconel 625. (c) Hastelloy X.

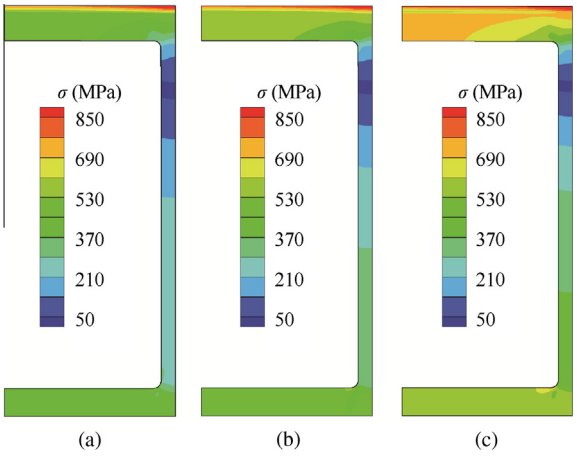

Fig. 10 Mises stress distribution at the outlet cross section of actively cooled panel with TBC. (a) Inconel X-750. (b) Inconel 625. (c) Hastelloy X.

allowable stress, so this material is safe. However, materials Inconel 625 and Hastelloy X are not within their safe working conditions since the stress is much larger than their allowable stress.

Considering both Figs. 6 and 9 we find that under the same thermal load, the temperature difference for the three materials is small while the stress difference is big. Inconel X-750 has the smallest stress among three materials, but Inconel 625 and Hastelloy X have much larger stresses. The Mises stress of materials depends predominantly on the thermal expansion coefficient and elasticity module. At the same time different materials have various mechanical characteristics. Inconel X-750 has a relatively high thermal conductivity and low elasticity module, so under the same heat load the Mises stress of Inconel X-750 is small, satisfying the requirement of the cooling channel. Meanwhile from Fig. 9 we can see that the stress at the top wall is large because the main heat transfer happens here and the maximum stress is at the top of the rib. One of the reasons is that the part is exposed directly to the combustor. The other reason is that the heat transfer is conducted from the top to the bottom part of the rib by conduction and with the coolants not providing a good convective heat transfer this results in the maximum stress in this area. It shows that the maximum stress happens at a position where the temperature does not reach its maximum value.

It can also be seen that the stress close to the combustor side is obviously bigger than at the side far from the combustor, which tells us that working conditions for the side close to the combustor are stricter, so the selection of the materials is dictated by the conditions in this area.

Therefore, a TBC with a 0.1 mm thickness is applied to the combustor's wall to protect the combustor. Fig. 10 gives the numerical Mises stress at the outlet cross section of the actively cooled panel with the TBC. It can be seen from the figure that the Mises stress is very high for the whole TBC layer since it contacts with the high temperature combustion gas and exchanges a lot of heat resulting in a much higher stress than that of the materials of the cooling channel. Although the stress is very high for the TBC, the mate-

Table 8 Analysis and numerical stress at main nodes of actively cooled panel with no TBC.

Material		Node stress (MPa)							
		1	2	3	4	5	6	7	8
Analysis	Thermal stress	578.0	578.0	548.9	548.9	563.4	563.4	563.4	563.4
	Mechanical stress	152.7	228.6	101.5	279.7	25.5	25.5	25.5	25.5
Simulation	Thermal stress	575.2	558.1	541.8	546.7	339.2	455.1	339.1	338.1
	Mechanical stress	121.0	165.3	113.4	210.6	28.3	34.3	29.8	21.9

Table 9 Analysis and numerical stress at main nodes of the actively cooled panel with TBC.

Material		Node stress (MPa)							
		1	2	3	4	5	6	7	8
Analysis	Thermal stress	556.1	556.1	528.1	528.1	542.1	542.1	542.1	542.1
	Mechanical stress	152.7	228.6	101.5	279.7	25.6	25.6	25.6	25.6
Simulation	Thermal stress	543.7	501.9	467.8	492.9	425.8	442.0	425.7	425.0
	Mechanical stress	125.0	176.2	115.7	218.4	28.5	33.6	29.8	21.9

rials' stress distribution is improved compared to the case with no TBC.

Considering both Figs. 7 and 10 we find that under the same thermal load, the Mises stress for Inconel X-750 is the smallest and for Hastelloy X it is the biggest. Comparing the cases of the three materials with no TBC, those with TBC have much lower Mises stresses close to the combustor. It indicates that the TBC delivers a great improvement for the materials at high temperature.

Since both the analytical and numerical methods can provide the stress distribution for a panel of the cooling system and the analytical method will save about 80% of the computing time, it is necessary to find out how well the results of these two methods agree with each other. Tables 8 and 9 show the comparison of the stress distribution between numerical and analytical results at the outlet cross section of the actively cooled panel for material Inconel X-750 with no TBC and with TBC respectively. The results show a similar trend for the distribution of the thermal stress and the mechanical stress. The value of mechanical stresses has a little discrepancy between the analysis and the simulation methods. The real structure of the actively cooled panel has round chamfers on the corners. The numerical simulation considers these chamfers, while the analytical method ignores these chamfers. So the stress concentration would occur at point 4, and the analytical value is bigger than the numerical values at point 4. The mechanical stress at point 4 affects the mechanical stresses at other points a lot, especially point 2. So the mechanical stress in analysis results is much bigger than that in simulation results.

5. Conclusion

(1) An analytic estimation and numerical modeling are performed to investigate the thermal and structural characteristics of actively cooled sandwich panels with Inconel X-750, Inconel 625 and Hastelloy X, three nickel alloys, with and with no TBC. The analytic model agrees well with finite element calculations.
(2) The part near the combustion chamber is the main working area of the active cooling system, the maximum temperature and stress all occurs in this section. So the part near the combustion chamber is the main area that should be considered for judging whether the materials will fail.
(3) Owing to Inconel X-750's high thermal conductivity and low Young's modulus of elasticity, the maximum temperature and stress in Inconel X-750 is lower than those in other materials for a certain channel structure and thermal load. Inconel X-750 is superior to the other two materials that could be used as the solid part of an active cooling system.
(4) With the addition of a TBC to the outside surface, which is exposed to the combustion chamber, the temperature of the channel does not significantly decrease, but the stress is reduced and is better distributed. In particular, the barrier coating provides a good protection for low yield strength materials such as Hastelloy X and it can improve the material's ability to withstand thermal loads.

Acknowledgments

The authors would like to thank the anonymous reviewers for their critical and constructive review of the manuscript. This study was co-supported by the Foundation for Innovative Research Groups of the National Natural Science Foundation of China (No. 51121004) and the Fundamental Research Funds for the Central Universities of China (No. HIT.BRETIV.201315).

References

1. Curran ET. Scramjet engines: the first forty years. *J Propul Power* 2001;**17**(6):1139–48.
2. Jin Y, He XM, Jiang B, Wu ZJ, Ding GY. Design and performance of an improved trapped vortex combustor. *Chin J Aeronaut* 2012;**25**(6):864–70.
3. Barnard P, Henderson MB, Rhodes N. CMC integration and demonstration for gas turbine engines (CINDERS). *Appl Therm Eng* 2004;**24**(11–12):1755–64.
4. Gori F, Corasaniti S, Worek WM, Minkowycz WJ. Theoretical prediction of thermal conductivity for thermal protection systems. *Appl Therm Eng* 2012;**49**(SI):124–30.
5. Liu JX, Hou ZX, Chen XQ, Zhang JT. Experimental and numerical study on the aero-heating characteristics of blunted waverider. *Appl Therm Eng* 2013;**51**(1–2):301–14.
6. Lu TJ. Heat transfer efficiency of metal honeycombs. *Int J Heat Mass Transf* 1999;**42**(20):31–40.
7. Lu TJ, Valdevit L, Evans AG. Active cooling by metallic sandwich structures with periodic cores. *Prog Mater Sci* 2005;**50**(7):789–815.
8. Gu S, Lu TJ, Evans AG. On the design of two-dimensional cellular metals for combined heat dissipation and structural load capacity. *Int J Heat Mass Transf* 2001;**44**(21):63–75.
9. Kim T, Hodson HP, Lu TJ. Fluid-flow and heat-transfer in ultralightweight lattice-frame materials. *Int J Heat Mass Transf* 2004;**47**(6):1129–40.
10. Tian J, Kim T, Lu TJ, Hodson HP, Queheillalt DT, Wadley HNG. The effects of topology upon fluid flow and heat-transfer within cellular copper structures. *Int J Heat Mass Transf* 2004;**47**(14):3171–86.
11. Lu HB, Liu WQ. Investigation of thermal protection system by forward-facing cavity and opposing jet combinatorial configuration. *Chin J Aeronaut* 2013;**26**(2):287–93.
12. Rakow JF, Waas AM. Thermal buckling of metal foam sandwich panels for convective thermal protection systems. *J Spacecr Rockets* 2005;**42**(5):832–44.
13. Maloney KJ, Fink KD, Schaedler TA, Kolodziejska JA, Jacobsen CS, Roper CS. Multifunctional heat exchangers derived from three-dimensional micro-lattice structures. *Int J Heat Mass Transf* 2012;**55**(9–10):2486–93.
14. Wang WX, Guo RW. Numerical study of unsteady starting characteristics of a hypersonic inlet. *Chin J Aeronaut* 2013;**26**(3):563–71.
15. Pirge G. Characterization of thermal barrier coated various aerospace alloys. *Aircr Eng Aerosp Technol* 2008;**80**(4):359–64.
16. Chen ZJ, Wang LL, Meng H. Study of heat transfer of cryogenic methane under supercritical pressure with consideration of thermal conduction in engine cooling channel walls. *Acta Aeronaut Astronaut Sin* 2013;**34**(1):8–18 Chinese.
17. Youn B, Mills AF. Cooling panel optimization for the active cooling system of a hypersonic aircraft. *J Thermophys Heat Transf* 1995;**9**(1):136–43.
18. Rakow JF, Waas AM. Response of actively cooled metal foam sandwich panels exposed to thermal loading. *AIAA J* 2007;**45**(2):329–36.

19. Rakow JF, Waas AM. Thermal buckling of metal foam sandwich panels for convective thermal protection systems. *J Spacecr Rockets* 2005;**42**(5):832–44.
20. Langener T, Wolfersdorf JV, Steelant J. Experimental investigations on transpiration cooling for scramjet applications using different coolants. *AIAA J* 2011;**49**(7):1409–19.
21. Song KD, Choi SH, Scotti SJ. Transpiration cooling experiment for scramjet engine combustion chamber by high heat fluxes. *J Propul Power* 2006;**22**(1):96–102.
22. Qin J, Zhang SL, Bao W, Jia ZJ, Yu B, Zhou WX. Experimental study on the performance of recooling cycle of hydrocarbon fueled scramjet engine. *Fuel* 2013;**108**:334–40.
23. Qin J, Bao W, Zhou WX, Yu DR. Flow and heat transfer characteristics in fuel cooling channels of a recooling cycle. *Int J Hydrog Energy* 2010;**35**(19):10589–98.
24. Bao W, Qin J, Zhou WX, Yu DR. Effect of cooling channel geometry on re-cooled cycle performance for hydrogen fueled scramjet. *Int J Hydrog Energy* 2010;**35**(13-SI):7002–11.
25. Kumar RR, Palaninathan R, Kishor E, Kumar GS, Deependran B. Role of thermal contact conductance on sandwich-type metallic thermal protection system profile. *AIAA J* 2012;**50**(10):2194–201.
26. Marren D, Lewis M, Maurice LQ. Experimentation, test, and evaluation requirements for future airbreathing hypersonic systems. *J Propul Power* 2001;**17**(6):1361–5.
27. Vermaak N, Valdevit L, Zok FW, Evans AG. Design and implementation of actively cooled panels for scramjets. *Proceedings of the ASME international mechanical engineering congress and exposition*; 2007 Nov 11–15; Seattle, WA, USA. New York: ASME Press; 2008. p. 191–7.
28. Vermaak N, Valdevit L, Evans AG, Zok FW, Mcmeeking RM. Implications of shakedown for design of actively cooled thermostructural panels. *J Mech Mater Struct* 2011;**6**(9):1313–27.
29. Vermaak N, Valdevit L, Evans AG. Influence of configuration on materials selection for actively cooled combustors. *J Propul Power* 2010;**26**(2):295–302.
30. Vermaak N, Valdevit L, Evans AG. Materials property profiles for actively cooled panels: an illustration for scramjet applications. *Metall Mater Trans A-Phys Metall Mater Sci* 2009;**40**(4):877–90.
31. Valdevit L, Pantano A, Stone HA, Evans AG. Optimal active cooling performance of metallic sandwich panels with prismatic cores. *Int J Heat Mass Transf* 2006;**49**(21–22):3819–30.
32. Valdevit L, Wei Z, Mercer C, Zok FW, Evans AG. Structural performance of near-optimal sandwich panels with corrugated cores. *Int J Solids Struct* 2006;**43**(16):4888–905.
33. Valdevit L, Hutchinson JW, Evans AG. Structurally optimized sandwich panels with prismatic cores. *Int J Solids Struct* 2004;**41**(18–19):5105–24.
34. Pizzarelli M, Nasuti F, Onofri M. CFD analysis of transcritical methane in rocket engine cooling channels. *J Supercrit Fluids* 2012;**62**:79–87.
35. Pizzarelli M, Nasuti F, Onofri M. Coupled wall heat conduction and coolant flow analysis for liquid rocket engines. *J Propul Power* 2013;**29**(1):34–41.
36. Kontinos D. Coupled thermal analysis method with application to metallic thermal protection panels. *J Thermophys Heat Transf* 1997;**11**(2):173–81.
37. Bao W, Li XL, Qin J, Zhou WX. Modelling and simulation methodology of channel cooling using hydrocarbon fuel as coolant under supercritical pressures. *Proc Inst Mech Eng Part G-J Aerosp Eng* 2011;**225**(G9):969–84.
38. Qin J, Bao W, Zhou WX, Yu DR. Performance cycle analysis of an open cooling cycle for a scramjet. *Proc Inst Mech Eng Part G-J Aerosp Eng* 2009;**223**(G6):599–607.
39. Hetnarski RB, Eslami MR. *Thermal stresses – advanced theory and applications: advanced theory and applications*. New York: Springer; 2008.
40. Ahmed SR, Idris ABM, Uddin MW. Numerical solution of both ends fixed deep beams. *Comput Struct* 1996;**61**(1):21–9.

Wang Xinzhi is a Ph.D. student at School of Energy Science and Engineering, Harbin Institute of Technology. He received his B.S. degree from Harbin Institute of Technology in 2013. His area of research includes functional fluid process intensification mechanism and application, and research of flow and heat transfer problems related to hypersonic flight vehicle.

He Yurong is a professor and Ph.D. supervisor at School of Energy Science and Engineering, Harbin Institute of Technology. She received the Ph.D. degree from the same university in 2004. Her current research interests are multiphase flow and heat transfer, functional fluid process intensification mechanism and application, research of flow and heat transfer problems related to hypersonic flight vehicle, and development and application of new energy.